Modelling Simul. Mater. Sci. Eng. **15** (2007) 369–384 doi:10.1088/0965-0393/15/3/013

Dauphiné twinning in polycrystalline quartz

Nathan R Barton[1] **and Hans-Rudolf Wenk**[2]

[1] Lawrence Livermore National Laboratory, PO Box 808, Livermore, CA 94551, USA
[2] University of California, Berkeley, Earth and Planetary Science, 497 McCone Hall, Berkeley, CA 94720-4767, USA

E-mail: barton22@llnl.gov

Received 6 November 2006, in final form 27 February 2007
Published 2 April 2007
Online at stacks.iop.org/MSMSE/15/369

Abstract

A recently developed crystal based continuum model for twinning and phase transformations is successfully applied to Dauphiné twinning and the α (trigonal) $\leftrightarrow$ β (hexagonal) phase transformation in quartz. Both finite element and uniform deformation simulations are performed of quartz polycrystals and several experimentally observed phenomena are qualitatively reproduced. Results are given for mechanically induced twinning and texture memory during phase transformation. The results highlight the importance of local stress variations due to grain interactions. Due to the form of the driving force, twinning is particularly sensitive to local stress variations.

1. Introduction

In the work reported here, we make use of recently developed material modelling capabilities to investigate Dauphiné twinning and the $\alpha \leftrightarrow \beta$ phase transformation in quartz. Due in part to its geological significance, quartz is of long standing interest, with Frondel [1] discussing the lattice orientation memory of single crystals during the $\alpha \leftrightarrow \beta$ transformation and Thomas and Wooster [2] investigating Dauphiné twinning under applied load. It has long been known that application of mechanical load can produce texture in a quartz polycrystal with an initially random orientation distribution [3]. Recent interest in the influence of stress and temperature on the activity of Dauphiné twinning in quartz is motivated by applications to tectonic deformation [4] and to shock deformation during meteorite impact [5,6]. Experimental work on quartz is ongoing and [7] describes some of the recent results which most directly motivate the modelling work reported here. References listed here are in no way meant to be exhaustive, though the references above do serve as a good starting point for the interested reader.

At room temperature and pressure α-quartz with trigonal crystal symmetry is the equilibrium phase. At higher temperature (above 573 °C at ambient pressure) β-quartz with hexagonal crystal symmetry becomes the stable phase. The α phase has two variants, which differ by small atomic displacements (on the scale of interatomic spacings). The reference

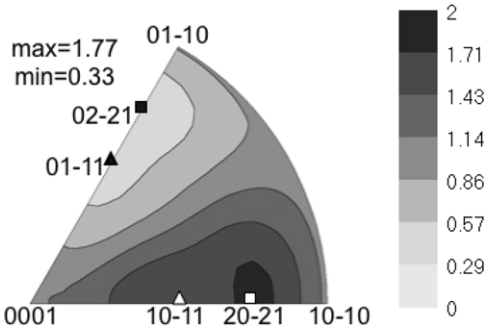

Figure 1. Fine-grained quartz rock novaculite deformed at 500 °C and a compressive stress of 600 MPa [7]. Inverse pole figure of the compression direction in MUD, drawn in equal area projection with a linear contour scale. Texture measurements were done with synchrotron x-rays at HASY and analysed with the Rietveld method MAUD.

lattices of these two α variants may be mapped into each other by a $\pi/3$ rotation about the c-axis of the crystal. The two variants can occur as twin intergrowths—following the so-called Dauphiné law. The Dauphiné twins formed in α quartz occur as both growth twins and as mechanical twins, with the intergrowth plane being generally irregular. From a modelling perspective, Dauphiné twinning and $\alpha \leftrightarrow \beta$ phase transformation in quartz are interesting because of the strong influence of non-hydrostatic stresses. For Dauphiné twinning there is no strain due to change in the reference lattice and all of the mechanical driving force arises from elastic anisotropy. This is because mechanical Dauphiné twinning is produced by local rearrangements of atoms without any larger scale shearing mechanism.

Similarly, elastic anisotropy is important in the $\alpha \leftrightarrow \beta$ phase transformation, particularly for α variant selection during cooling. The importance of these effects has been known for some time, with MacDonald [8] predicting that non-hydrostatic stresses are significant in the $\alpha \leftrightarrow \beta$ transformation. Implementations of general three-dimensional large strain continuum mechanics models of phase transformation and twinning have not, however, typically included the appropriate elastic anisotropy effects. Here we build on a recently developed model which does include lattice strain and elastic anisotropy effects [9,10]. Other notable models which can treat these effects include those presented in [11,12]. Though they do not necessarily include the effects of elastic anisotropy, various other efforts further highlight the importance of complex local strain fields in driving phase transformation and twinning; see for example [13, 14].

The work on quartz reported here is motivated in large part by two experimental observations for which we wish to have a quantitative observation. As was documented in [7, 15], if a quartz rock without preferred orientation is subjected to a compressive stress, a characteristic texture pattern develops that has been attributed to mechanical twinning. An example is shown in figure 1 with an inverse pole figure of the compression direction. Regions around negative rhombs (such as $(0\,2\,\bar{2}\,1)$) become depleted and regions around positive rhombs (such as $(2\,0\,\bar{2}\,1)$) become enforced. The c-axes $(0\,0\,0\,1)$ and prism planes $(1\,0\,\bar{1}\,0)$ do not develop preferred orientation.

This twinning effect has also been observed by neutron diffraction when compressing a sample *in situ* and observing intensity changes in the diffraction pattern (figure 2). The intensity of $(1\,0\,\bar{1}\,0)$ does not change because this reflection is insensitive to twinning. Intensities of rhombohedral reflections such as $(1\,0\,\bar{1}\,2)$ change profoundly and, as can be seen, Dauphiné twinning initiates around 80 MPa and saturates around 500 MPa. Upon unloading some of the twinning is reversed.

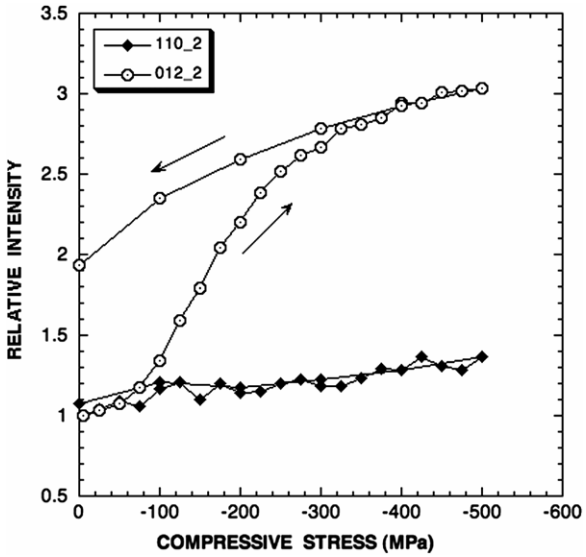

Figure 2. Novaculite deformed in compression at 500 °C in the time-of-flight neutron diffractometer SMARTS at LANSCE. The intensity change of $(1\,0\,\bar{1}\,2)$ as a function of applied stress is indicative of mechanical twinning.

The results presented here emphasize Dauphiné twinning, with further work planned to investigate the phase transformation in more detail. Details of the phase transformation are complex and not completely understood [16, 17]. To some degree these details are not important for continuum level modelling and with relatively simple assumptions we are able to highlight the importance of local stress state in the phase transformation. That is, certain general conclusions may be reached even though the model does not capture in detail the transient phenomena occurring during the phase transformation.

2. Material model

We make use of a model that treats phase and twinning transformations and which has been applied to the $\alpha \leftrightarrow \epsilon$ transformation in iron [10]. In this model, each material element is made up of microstructural constituents, with each constituent having its own mass fraction. Stress and temperature equilibrium are assumed among the constituents. For the application to quartz, the microstructure is composed of three constituents, with transformation paths between each of them, as indicated in figure 3. We will use transformation as a generic term for either a twinning transformation or a phase change transformation. Counting both forward and reverse transformations, there are six paths in the model for quartz.

Each constituent has its own lattice orientation, with anisotropic properties oriented with respect to that lattice. For the current application to quartz it is the elastic anisotropy which is of primary concern. Under the conditions of interest, it is safe to assume that the constituents do not themselves deform plastically by mechanisms such as dislocation glide. Such plastic deformation would bring in additional anisotropy associated with the lattice of each constituent. Dislocation glide mechanisms may be included in the model and were considered in the investigation of iron [10].

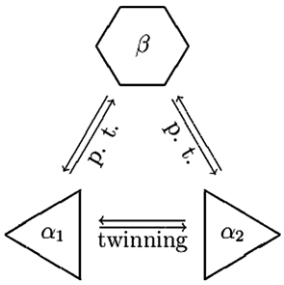

Figure 3. Microstructural constituents and transformation paths; geometric shapes indicate crystallographic symmetry, not atomic positions.

2.1. Kinematics and driving forces

Forms for the kinematics and the driving forces are identical to those in [10]. For Dauphiné twinning, we adopt a form of kinetics that is better able to capture temperature effects. For convenience, key equations are summarized here before introducing the new kinetics.

Within each constituent, we perform a multiplicative decomposition of the constituent deformation gradient:

$$\boldsymbol{F} = \boldsymbol{V} \cdot \boldsymbol{R} \cdot \boldsymbol{F}^{\mathrm{P}}. \tag{1}$$

Lattice rotation is captured by the proper rotation $\boldsymbol{R}$ and $\boldsymbol{V}$ is a symmetric tensor including both thermal and elastic stretch of the lattice. If plastic deformation by dislocation glide were allowed, then these deformations would be captured by $\boldsymbol{F}^{\mathrm{P}}$. While simulations have been conducted with dislocation glide in the β phase at high temperature in order to examine the effects on establishment of a residual stress state, none of these results are included here.

Let constituents be indicated by Greek indices, with all summations over constituents indicated explicitly. With constituent volume fraction v_ζ and velocity gradient $\boldsymbol{L}_\zeta$ in constituent ζ, the total apparent velocity gradient is

$$\langle \boldsymbol{L} \rangle = \boldsymbol{L}^{\chi} + \sum_{\zeta} v_\zeta \boldsymbol{L}_\zeta, \qquad \boldsymbol{L}^{\chi} = \sum_{i} \boldsymbol{L}_{(i)} \tag{2}$$

with $\boldsymbol{L}^{\chi}$ containing contributions due to transformations. Within each constituent ζ, the velocity gradient $\boldsymbol{L}_\zeta$ arises from the deformation gradient in equation (1) formed with quantities specific to constituent ζ. Thus $\boldsymbol{L}_\zeta$ captures all non-transformation deformation mechanisms for constituent ζ. Volume fractions v_ζ in the above equation are related to mass fractions through the current densities of the constituents [10].

For each transformation path i taking mass from constituent $\eta_{\mathrm{fr}}(i)$ to constituent $\eta_{\mathrm{to}}(i)$ with mass fraction rate $\dot{m}_{(i)}$, $\boldsymbol{L}^{\chi}$ has a contribution of the form

$$\boldsymbol{L}_{(i)} = \dot{m}_{(i)}[\boldsymbol{V}_{\eta_{\mathrm{to}}(i)} \cdot \hat{\boldsymbol{G}}_{(i)} \cdot (\boldsymbol{V}_{\eta_{\mathrm{fr}}(i)})^{-1} + \boldsymbol{V}_{\eta_{\mathrm{to}}(i)} \cdot (\boldsymbol{V}_{\eta_{\mathrm{fr}}(i)})^{-1} - \boldsymbol{I}], \tag{3}$$

where $\boldsymbol{V}_\zeta$ are the constituent lattice deformations. The term involving $\hat{\boldsymbol{G}}_{(i)}$ captures straining due to changes in the reference positions of atoms in the lattice, with $\hat{\boldsymbol{G}}_{(i)}$ in general depending on the current constituent mass fractions m_η. For Dauphiné twinning in α quartz, there is no strain associated with changes in the reference positions and $\hat{\boldsymbol{G}}_{(i)}$ is always zero.

For the $\alpha \leftrightarrow \beta$ phase transformation, $\hat{\boldsymbol{G}}_{(i)}$ brings in the effects of changes in the a and c lattice parameters on transformation. Due to kinematics, $\hat{\boldsymbol{G}}_{(i)}$ depends on the current mass fractions [10], but the dominant factor depends directly on the lattice parameters. For $\alpha \rightarrow \beta$

transformation, the dominant factor in $\hat{\boldsymbol{G}}_{(i)}$ has components in the reference crystal lattice frame with just the diagonal entries $(a_\beta/a_\alpha - 1, a_\beta/a_\alpha - 1, c_\beta/c_\alpha - 1)$.

The driving force for transformation is written as

$$f_{(i)} = f^{\mathrm{d}}_{(i)} - C_{(i)} \cdot (\theta - \theta^{\mathrm{o}}_{(i)}), \tag{4}$$

where $\theta^{\mathrm{o}}_{(i)}$ is the so-called equilibrium temperature for the phase transformation and $f^{\mathrm{d}}_{(i)}$ is the driving force due to the action of the stress. For the $\alpha \leftrightarrow \beta$ phase transformation, the second term in the above equation captures the effect of temperature dependent differences in free energy in the bulk states of the phases. For Dauphiné twinning, there is no direct temperature contribution to the driving force and the second term vanishes. Temperature does still indirectly influence the driving force through thermal anisotropy and its effects on internal stress state in a polycrystal. Note that the form in equation (4) does not include any contributions from mixtures of mass fractions within a given material element. For now we assume that any boundary or interaction energies that would result in such contributions are comparatively small.

The mechanical driving force has the form

$$f^{\mathrm{d}}_{(i)} = \boldsymbol{\tau}_{\eta_{\mathrm{fr}}(i)} : \boldsymbol{P}_{(i)} \tag{5}$$

with $\boldsymbol{\tau}_{\eta_{\mathrm{fr}}(i)}$ being the Kirchhoff stress per reference volume in the transforming constituent and

$$\boldsymbol{P}_{(i)} = \mathrm{symm}\ (\ln(\boldsymbol{F}_{(i)})). \tag{6}$$

The quantity $\boldsymbol{F}_{(i)}$ indicates the total deformation gradient on transformation for path i. For the $\alpha \leftrightarrow \beta$ phase transformation the change in reference lattices contributes significantly to $\boldsymbol{P}_{(i)}$, with

$$\boldsymbol{F}_{(i)} = \boldsymbol{V}_{\eta_{\mathrm{to}}(i)} \cdot \hat{\boldsymbol{F}}^{*}_{\eta_{\mathrm{to}}(i)} \cdot (\hat{\boldsymbol{F}}^{*}_{\eta_{\mathrm{fr}}(i)})^{-1} \cdot (\boldsymbol{V}_{\eta_{\mathrm{fr}}(i)})^{-1} \tag{7}$$

and $\hat{\boldsymbol{F}}^{*}_{\eta_{\mathrm{to}}(i)}$ and $\hat{\boldsymbol{F}}^{*}_{\eta_{\mathrm{fr}}(i)}$ indicating the deformation gradients for the reference lattices in the product and source phases, respectively. For $\alpha \to \beta$ transformation, components of $\hat{\boldsymbol{F}}^{*}_{\eta_{\mathrm{to}}(i)} \cdot (\hat{\boldsymbol{F}}^{*}_{\eta_{\mathrm{fr}}(i)})^{-1}$ in the reference crystal lattice frame consist of just the diagonal entries $(a_\beta/a_\alpha, a_\beta/a_\alpha, c_\beta/c_\alpha)$. Components for the reverse transformation are simply the reciprocals of the foregoing. Note that if one neglected the effects of lattice stretches $\boldsymbol{V}_{\eta_{\mathrm{to}}(i)}$ and $\boldsymbol{V}_{\eta_{\mathrm{fr}}(i)}$ and used a small strain approximation, components of $\boldsymbol{P}_{(i)}$ would reduce to $(a_\beta/a_\alpha - 1, a_\beta/a_\alpha - 1, c_\beta/c_\alpha - 1)$ in the reference crystal lattice frame.

The form chosen in equation (6) is motivated in part by considerations for transformations in which the effects of volume change and thus pressure are more pronounced than those here [10]. As discussed in [10], equation (6) is developed by considering an integral form of the deformation portion of the driving force, motivated in part by the work in [18]. The form is consistent with the assumption that the microstructural constituents are in stress equilibrium. If instead jump conditions and compatibility requirements were enforced on an explicit moving phase boundary, other forms might be appropriate [19]. For further discussions of the development of driving forces for phase transformation and twinning, see for example the work in [11, 20, 21].

For the special case of a Dauphiné twinning transformation mode, $\hat{\boldsymbol{F}}^{*}_{\eta_{\mathrm{to}}(i)} \cdot (\hat{\boldsymbol{F}}^{*}_{\eta_{\mathrm{fr}}(i)})^{-1} = \boldsymbol{I}$ exactly. Thus $\boldsymbol{F}_{(i)} = \boldsymbol{V}_{\eta_{\mathrm{to}}(i)} \cdot (\boldsymbol{V}_{\eta_{\mathrm{fr}}(i)})^{-1}$ and $\boldsymbol{P}_{(i)}$ involves only the lattice strains. These lattice strains are related to the stress through the anisotropic thermo-elastic response, with the anisotropy being specific to the crystal orientation of each variant. Changes in elastic moduli (with respect to a given reference frame) therefore enter into the mechanical driving force. The leading term of $\boldsymbol{P}_{(i)}$ is then linear in the lattice strains, so that the leading term of $f^{\mathrm{d}}_{(i)}$ is quadratic in the stress. This makes the Dauphiné twinning transformations particularly

sensitive to changes in the local state of stress. In contrast, the $\alpha \leftrightarrow \beta$ transformation modes have a term in $f^{\mathrm{d}}_{(i)}$ which is linear in the applied stress. If isotropic thermo-elastic properties were used then stress equilibrium would produce $\boldsymbol{V}_{\eta_{\mathrm{to}}(i)} = \boldsymbol{V}_{\eta_{\mathrm{fr}}(i)}$ so that $f^{\mathrm{d}}_{(i)} = 0$ and the driving force for Dauphiné twinning would be eliminated. Thermo-elastic anisotropy plays a central role in the Dauphiné twinning driving force.

2.2. *Dauphiné twinning kinetics*

The Dauphiné twinning kinetics follow a form motivated by considerations from statistical mechanics [22, 23], and are similar in some regards to the mechanical threshold stress formalism used in dislocation glide based plasticity modelling [24]. Based on the computed form of the potential energy curves along the α_1-β-α_2 twinning path [25, 26], we assume that the barrier height for twinning decreases as the temperature increases towards the $\alpha \rightarrow \beta$ transformation temperature. A decrease in activation energy near the transformation temperature is also consistent with experimental observations of extensive small scale twinning near the transformation temperature [27].

Considering a specific Dauphiné twinning mode for which $f \geqslant 0$, the mass fraction rate motivated by statistical mechanics could have the standard form

$$\dot{m} = \Phi^{\mathrm{o}} \exp\left(-\frac{\Delta G}{k \cdot \theta}\right). \tag{8}$$

For simplicity we neglect any temperature variation of $\dot{\Phi}^{\mathrm{o}}$, approximating it as a constant [23]. Assuming a simple bilinear form for ΔG, we write

$$\Delta G(f, \theta) = (g^{\mathrm{o}} + \theta \cdot g^{\theta})\left(1 - \frac{f}{\xi^{\mathrm{o}}_{\mathrm{tw}}}\right) \tag{9}$$

in which g^{o}, g^{θ}, and $\xi^{\mathrm{o}}_{\mathrm{tw}}$ are constants. The temperature variation of ΔG is meant to capture the change in barrier height for twinning as the material approaches the $\alpha \rightarrow \beta$ temperature. This gives a temperature variation in ΔG which is stronger than that typically used in other contexts where ΔG is scaled by temperature variation in the shear modulus, as in [28]. Some other functional form for ΔG may ultimately prove superior in capturing the relevant physics, but for now equation (9) suffices.

An issue does however remain with the form of equation (8) for the mass fraction rate. Specifically, the equation gives non-zero $\dot{m}$ at zero f. Numerically, the mass fraction rate is effectively zero at small temperatures. But this does not hold at higher temperatures. The physical significance is that at high temperatures thermal fluctuations are able to drive the twinning transformation if the driving force is negligible or even negative. We therefore use a balanced form like that found in [29]:

$$\dot{m} = \Phi^{\mathrm{o}}\left[\exp\left(-\frac{\Delta G(f, \theta)}{k \cdot \theta}\right) - \exp\left(-\frac{\Delta G(-f, \theta)}{k \cdot \theta}\right)\right]. \tag{10}$$

This accounts for both forward and reverse senses of the given transformation, and results in $\dot{m}$ being exactly zero when f is zero for all θ. The form in equation (10) is effectively a hyperbolic sine function in f, but this would not necessarily be the case with a more complex functional form for ΔG.

Figure 4 illustrates the above issue with the kinetics. At relatively low temperatures, both forms for the kinetics effectively give zero mass fraction rate until the relative driving force $(f/\xi^{\mathrm{o}}_{\mathrm{tw}})$ is nearly unity. At such low temperatures, the 'balanced' (equation (10)) and 'unbalanced' (equation (8)) forms of the kinetics are indistinguishable by eye. For higher temperatures, the balanced and unbalanced kinetics give similar results at larger relative driving

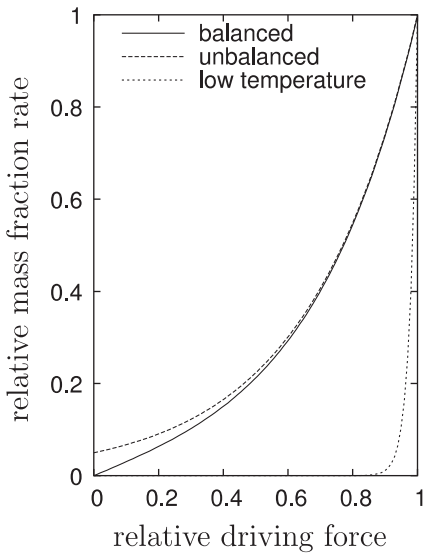

Figure 4. Mass fraction rate kinetics, highlighting the difference between balanced and unbalanced kinetics at high temperatures. At relatively low temperatures the two forms produce virtually identical results.

forces but the balanced kinetics are smooth through the origin while the unbalanced kinetics have a jump if negative driving forces are considered. This is a truly important consideration given that the twinning transformation is reversible. Due to the form of the mechanical driving force in equation (6), driving forces for the forward and reverse twinning paths are the negatives of each other.

2.3. $\alpha \leftrightarrow \beta$ phase transformation kinetics

Given that the kinetics for $\alpha \leftrightarrow \beta$ phase transformation are not expected to be as temperature sensitive, we simply use a power-law form:

$$\dot{m} = \Phi^{\mathrm{o}} \left(\frac{f}{\xi^{\mathrm{o}}_{\mathrm{pt}}} \right)^{1/p} . \tag{11}$$

For the results reported here, the resistance $\xi^{\mathrm{o}}_{\mathrm{pt}}$, the rate sensitivity p, and the reference rate $\dot{\Phi}^{\mathrm{o}}$ are all taken to be the same constants for forward and reverse transformation. Note that forward and reverse transformations are considered separately, so that equation (11) is used only for $f \geqslant 0$. Power-law forms are routinely used in transformation models [30–32]. Discussions of some of the complexities of the $\alpha \leftrightarrow \beta$ phase transformation are given for example in [16,17]. Details of the texture memory results presented below do not seem to be sensitive to the details of the transformation kinetics.

2.4. Thermo-elastic response

Quantities in this section refer to a particular constituent. For example, e denotes the specific internal energy of the constituent in question. The relation $\boldsymbol{\tau} = f_{\mathcal{K}}(\hat{\boldsymbol{E}}, e)$ governs the elastic response, with the Kirchhoff stress $\boldsymbol{\tau}$ related to the Cauchy stress $\boldsymbol{\sigma}$ by $\boldsymbol{\tau} = J\boldsymbol{\sigma}$. More

Table 1. Material parameters for α-quartz (trigonal), with reference values at $\theta^{\mathrm{o}} = 846$ K. Elastic moduli and their temperature derivatives are in units of GPa and GPa K^{-1}, respectively.

c_{11}	c_{12}	c_{13}	c_{14}	c_{33}	c_{44}	
68	−21	−6	−14	80	42	
$c_{11,\theta}$	$c_{12,\theta}$	$c_{13,\theta}$	$c_{14,\theta}$	$c_{33,\theta}$	$c_{44,\theta}$	
−0.034	−0.051	−0.033	0.0071	−0.050	−0.029	
S	$\Gamma_{\mathrm{o}11}$	$\Gamma_{\mathrm{o}33}$	c_v (kJ kg^{-1} K^{-1})	$\bar{\rho}$ (g cm^{-3})	c/a	a (Å)
0.5	1.87	1.53	0.295	2.5334	1.0938	4.978

specifically,

$$\begin{aligned} \boldsymbol{\tau}' &= \mathcal{K}' : \hat{\boldsymbol{E}} - \bar{\rho} e \boldsymbol{\Gamma}', \\ \mathrm{tr}(\boldsymbol{\tau}) &= -3 J p_{\mathrm{b}} + \boldsymbol{K} : \hat{\boldsymbol{E}}' \end{aligned} \tag{12}$$

in which $\boldsymbol{\Gamma}'$ is the deviatoric part of the constant second order Grüneisen tensor. $\mathcal{K}'$ and $\boldsymbol{K}$ are fourth order and second order elastic moduli tensors which depend on temperature. In the modelling framework, the elastic moduli may also depend on p_{b} (the bulk pressure), but these effects are not included for now given the small pressure excursions of interest here. $\bar{\rho}$ is the reference density ($E = \bar{\rho} e$).

With the chosen Mie–Grüneisen equation of state, pressure due to volumetric strain, or bulk pressure, takes the form

$$p_{\mathrm{b}}(\mu, e) = p_{\mathrm{g}}(\mu) + \bar{\rho} \mathrm{e} \Gamma, \tag{13}$$

where

$$p_{\mathrm{g}}(\mu) = \frac{K_{\mathrm{o}} \mu \left[1 + (1 - \frac{\Gamma_{\mathrm{o}}}{2})\mu - \frac{a\mu^2}{2} \right]}{[1 - (S-1)\mu]^2} \qquad \text{in compression} \tag{14}$$

$$p_{\mathrm{g}}(\mu) = K_{\mathrm{o}} \mu \qquad \text{in tension.} \tag{15}$$

$\Gamma = \mathrm{tr}(\boldsymbol{\Gamma})$ is the Grüneisen coefficient and μ is the compression. Typically obtained from particle velocity versus shock velocity data, S influences the change in bulk modulus with compression.

Specific internal energy within a constituent is determined from the total specific internal energy and the assumption of thermal equilibrium among constituents. Anisotropic thermal expansion occurs due to the appearance of the internal energy in the expression for the stress.

2.5. Material parameters

Tables 1–3 contain material parameters used in the simulations discussed below. These parameters are obtained from a variety of sources, and reference conditions are taken to be the assumed equilibrium phase transformation temperature, θ^{o}. Elasticity data are approximated from [33–36]. The work of Coe and Patterson [35] also has experimental data for transformation stress versus temperature at various lattice orientations, and this data is used to calibrate C. Lattice parameters and thermal expansion ($\boldsymbol{\Gamma}$) data are drawn from [37]. Other parameters are simply set to achieve physically reasonable behaviour. Parameters are obtained by fitting overall temperature variation in the vicinity of θ^{o}, not by using the θ^{o} values directly.

Table 2. Material parameters for β-quartz (hexagonal), with reference values at $\theta^{\mathrm{o}} = 846\,\mathrm{K}$. Elastic moduli and their temperature derivatives are in units of GPa and GPa K^{-1}, respectively.

c_{11}	c_{12}	c_{13}	c_{33}	c_{44}	
110	11	36	103	34	
$c_{11,\theta}$	$c_{12,\theta}$	$c_{13,\theta}$	$c_{33,\theta}$	$c_{44,\theta}$	
0.090	0.091	0.055	0.083	0.020	
S	$\Gamma_{\mathrm{o}11}$	$\Gamma_{\mathrm{o}33}$	c_v (kJ kg^{-1} K^{-1})	c/a	a (Å)
0.5	0	0	0.295	1.09216	4.9965

Table 3. Material parameters for twinning and phase transformation.

C (MPa K^{-1})	θ^{o} K	p	$\dot{\Phi}^{\mathrm{o}}$ ($\mu\mathrm{s}^{-1}$)	$\xi^{\mathrm{o}}_{\mathrm{pt}}$ (MPa)
−0.0447	846	0.05	10^2	0.05
g^{o}/κ(K)	g^{θ}/κ	$\xi^{\mathrm{o}}_{\mathrm{tw}}$(MPa)		
76583	−80.52	0.15		

2.6. Numerics and time integration for state update

The numerical procedure is the same as that described in [10]. To solve the constitutive update problem, we must solve a nonlinear set of equations subject to various constraints. The nonlinear equations satisfy equation (2) and mass conservation for each constituent. The overall approach is based on solution of the trust region subproblem using the subspace method, with an active set approach for handling bound constraints on the mass fractions [38]. An equality constraint forces the mass fractions to sum to unity at every iteration in the nonlinear solution process. With non-linearities in the stress and temperature equilibrium being relatively mild, linearization is used to condense out non-essential degrees of freedom. Corrections are then performed as needed during iteration to enforce the equilibrium constraints.

While state in each portion of material is updated according to the above procedure, grain interactions in a polycrystal can be modelled using a variety of methods. Here we employ both the finite element method and a uniform deformation (extended Taylor) linking assumption. For the uniform deformation linking assumption, the constitutive update numerical procedure is employed within each grain in the polycrystal. Under the finite element method, we invoke the numerical procedure at each integration point in the finite element discretization of the polycrystal.

3. Simulations and results

Many simulation details are motivated by recent experimental work performed on novaculite [7]. Novaculite is a fine grained dense quartz rock from Arkansas, with roughly equiaxed grain structure, no initial preferred orientation (texture), minimal porosity and no significant residual stresses. It is a sedimentary rock that did not undergo tectonic deformation. Simulation details here are not exactly the same as experimental conditions in [7]. We do not, for example, apply confining pressure. The sequence of thermal and mechanical loading is also not identical. At the current stage of development, we are exercising the model to verify that it qualitatively produces experimentally observed behaviours.

For simplicity of presentation, all simulation results presented here involve a polycrystal containing 512 grains. These grains start from a stress free state at 300 K and are initially untwinned—all mass is initially associated with constituent α_1. Initial lattice orientations are sampled from a uniform orientation distribution function (ODF), and the same set is used in all simulations.

3.1. Dauphiné twinning

In these simulations, the polycrystal is first heated with traction free external surfaces. While no external loads are applied, internal stresses develop due to the thermal anisotropy of the material. At fixed temperature, the material is then axially compressed to an average axial compressive stress of roughly 600 MPa and then unloaded. During this compression cycle, the lateral faces remain traction free. Most results are from the case in which the polycrystal is heated from 300 to 773 K before application of mechanical load. Finally, the temperature is cycled up to 950 K and back down to cycle the material through the $\alpha \leftrightarrow \beta$ phase transformation, with all surfaces once again traction free during this final thermal cycle. Throughout the simulation, temperature in the polycrystal is forced to be isothermal.

Finite element simulations are conducted using an idealized microstructure with $4 \times 4 \times 4$ brick finite elements in each initial α grain. This results in roughly thirty-three thousand finite elements[3]. The computational expense of the material model makes this a sizable computational task for current computer resources and the simulations are run in parallel using the `ale3d` finite element code [39]. A mesh refinement study was performed using a smaller polycrystal to verify that the number of elements per grain is sufficient. Preliminary studies also indicate that use of an idealized grain shape does not substantially influence results.

Simulations of the polycrystal are also performed using a uniform deformation (extended Taylor) linking assumption. Traction boundary conditions are satisfied by adjusting the velocity gradient at each time step to satisfy conditions imposed on the volume average stress components. These simulations are much less computationally expensive, but, as we will see below, do not capture all the important effects.

Texture results are conveniently presented in terms of compression axis inverse pole figures [40]. These pole figures show the tendency of crystallographic directions to be aligned with the compression direction. While general large lattice rotations are allowed in the model, lattice rotations remain small under the current conditions because there is not plastic deformation by dislocation glide mechanisms. All visible texture evolution is therefore associated with twinning. At each material point, the volume fractions of α_1 and α_2 become weights in the contribution to the inverse pole figure. All inverse pole figures are shown in equal area projection with the same scale used in all figures: 0 to 3 multiples of a uniform distribution (MUD). Due to the nature of the twinning modes being considered and the lack of other plastic deformation mechanisms, the peak inverse pole figure MUD value is 2 when starting from a uniform ODF. However, our 512 grain sample only approximates a uniform ODF and it is therefore possible for inverse pole figure MUD values to be greater than 2. In general, the lack of smoothness in the inverse pole figures is due to the finite aggregate size. Inverse pole figures are generated directly from the simulation data, without intermediate construction of an ODF.

Figures 5 and 6 contain inverse pole figures for finite element and uniform deformation simulations, respectively. Figures 5(*a*) and 6(*a*), showing material at 773 K before mechanical loading, are largely indicative of the initial texture. There is limited twinning in the finite

[3] The simulation took approximately 105 wall-clock hours on 64 processors (with 2.4 GHz CPU speed) for a total of 6720 CPU-hours.

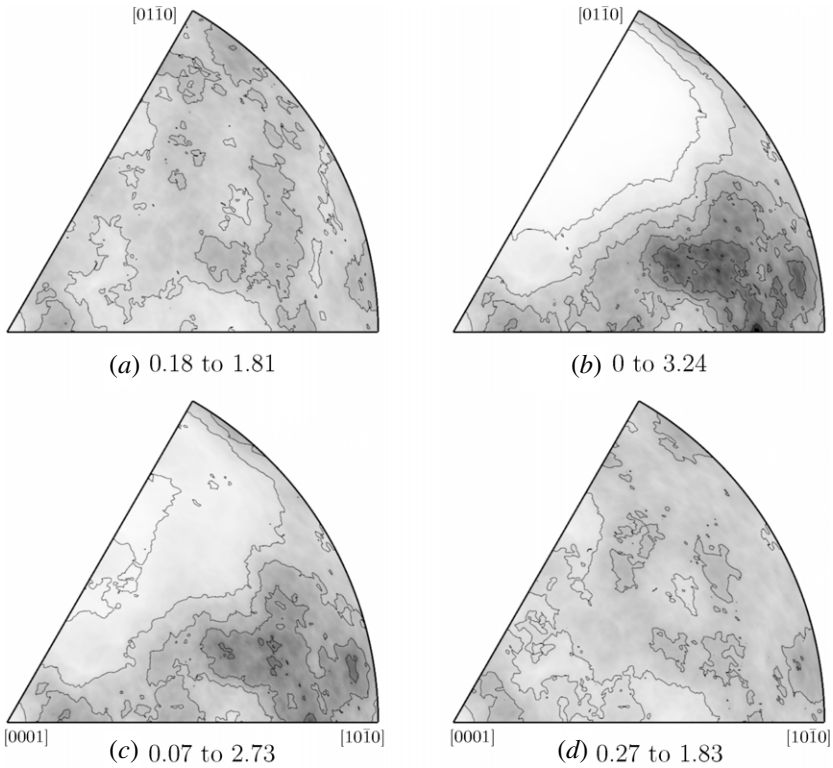

Figure 5. Finite element results. Compression axis inverse pole figures in equal-area projection, all at 773 K (*a*) before loading, (*b*) at peak compressive load, (*c*) after unloading and (*d*) after thermal cycling through the $\alpha \leftrightarrow \beta$ transformation. All plots use a scale from 0 to 3 MUD; data adjacent to plot labels give the value range of the actual data.

element simulation, particularly at grain boundaries, due to thermal stresses; and this accounts for differences between the inverse pole figures. Under peak compressive load (figures 5(*b*) and 6(*b*)) the material has undergone more extensive twinning, with a clear shift of poles from the vicinity of $(0\,2\,\bar{2}\,1)$ to the vicinity of $(2\,0\,\bar{2}\,1)$. This trend is a direct consequence of the elastic anisotropy of the α phase combined with this particular overall loading.

We see from figure 5(*c*) that the finite element simulation predicts some reversal of twinning upon unloading. The uniform deformation result (figure 6(*c*)) on the other hand does not predict any significant reversal of the twinning. Interactions among the grains create complex local stress fields within the grains and these seem to be important in capturing this particular effect. The twinning resistance parameter, ξ^{o}_{tw}, is also very important in regulating this effect. Increases in ξ^{o}_{tw} increase the hysteresis between the $\alpha_1 \rightarrow \alpha_2$ and $\alpha_2 \rightarrow \alpha_1$ modes, making it less likely that twin reversal will occur upon unloading. Preliminary *in situ* loading experiments using neutron diffraction have shown some twinning reversal and the value of ξ^{o}_{tw} used here is chosen to produce a roughly similar amount of reversal in the finite element simulations (figure 2).

Finally, figures 5(*d*) and 6(*d*) show the inverse pole figures after cycling though the $\alpha \leftrightarrow \beta$ phase transformation. While the material is still significantly twinned, the preferred orientation distribution developed by mechanical loading in the α phase has been lost. This phenomenon is discussed in more detail below in section 3.2.

Histories of the twinning as a function of thermo-mechanical loading also provide interesting insights. Figure 7 contains histories from the finite element simulation. These

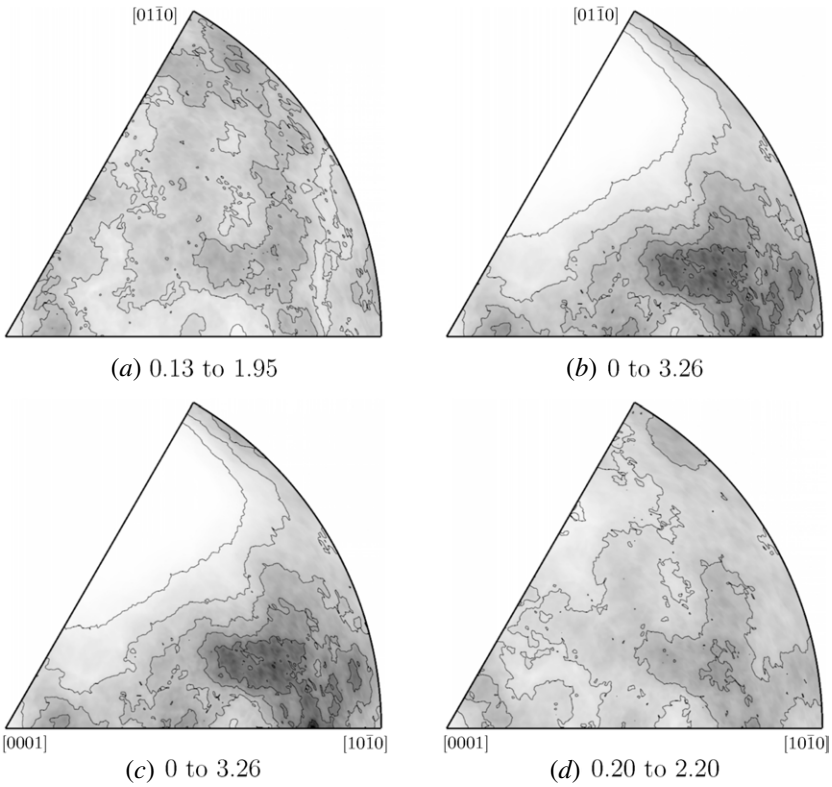

Figure 6. Uniform deformation simulation results. Compression axis inverse pole figures in equal-area projection, all at 773 K (*a*) before loading, (*b*) at peak compressive load, (*c*) after unloading and (*d*) after thermal cycling through the $\alpha \leftrightarrow \beta$ transformation. All plots use a scale from 0 to 3 MUD; data adjacent to plot labels give the value range of the actual data.

plots simply show the volume average of the amount of α_2. Recall that all material begins in the α_1 variant, and that the material is first heated (figure 7(*a*)) and then mechanically loaded (figure 7(*b*)). As may be noted from figure 7(*a*), some twinning occurs during heating from room temperature. This twinning is concentrated at grain boundaries and corners, where stresses produced by thermal anisotropy are highest. The development of thermal stresses is not the only factor in this effect—twinning becomes easier with increasing temperature due to the form of the twinning kinetics. Twinning due to thermal stresses is consistent with the experimental observations by [1] that temperature changes can cause twinning even if the temperature does not rise and fall through the transformation temperature. Figure 7(*b*) shows histories of twin fraction during mechanical load at two temperatures. During the application of mechanical load, some small portion of the twins that are already formed due to thermal stresses revert, but the dominant effect is to produce more twins. After an initial lag as stresses increase, the average twin fraction increases and then begins to saturate. Both the lag and saturation are experimentally observed phenomena [7]. For this material with uniform initial texture, it is only after load is applied that the twinning becomes systematic and produces texture. During unloading, there is relatively little change in the volume averaged amount of α_2, but we know from figure 5(*c*) that the ODF changes significantly upon unloading in the 773 K simulation. Differences with temperature in figure 7(*b*) are not as strong as

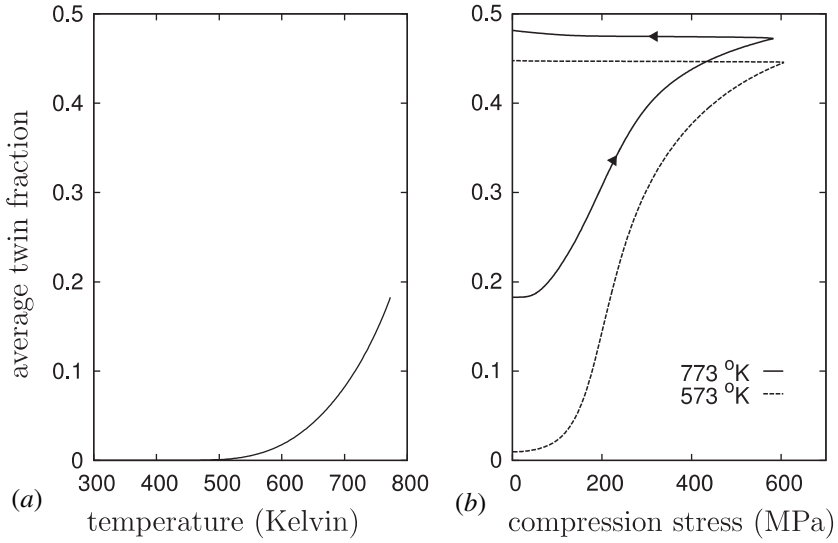

Figure 7. Average twin fraction evolution, versus (*a*) isothermal temperature without applied external load and then (*b*) volume average compression stress at fixed temperature.

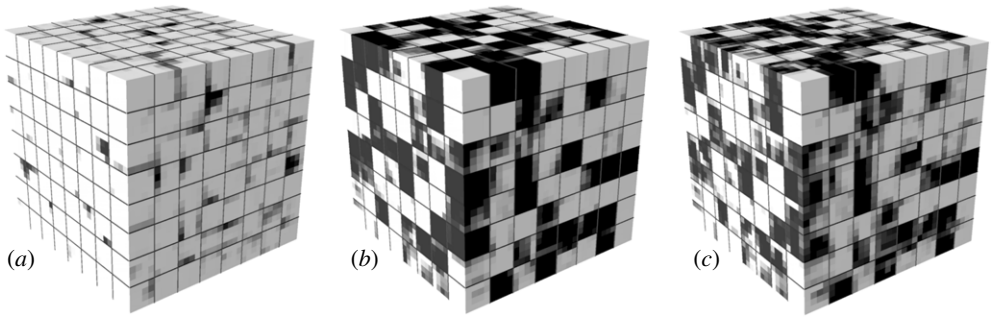

Figure 8. Mesh plots of twinned (dark) and untwinned (light) regions at (*a*) end of heating to 500 °C, (*b*) end of loading and (*c*) end of unloading.

those observed experimentally [7], indicating room for improvement in the kinetics and the temperature dependent material parameters.

For both loading and unloading, histories of the driving force for twinning in particular material elements (not shown) are not necessarily monotonic. This is a reflection of both the nonlinear dependence of the driving force on stress and grain interactions. Non-monotonicity of the driving forces bears directly on the saturation of twinning before all grains that are seemingly oriented for twinning do in fact twin.

It is also useful to examine plots of the twinning over the physical domain, and such plots are contained in figure 8. From figure 8(*b*), we see that under load some grains have twinned completely while others experience only partial twinning. Grain interactions may in some cases prevent complete twinning of grains that would, based on their lattice orientation and the overall state of stress, twin completely. Comparison of figures 8(*b*) and (*c*) highlights the fact that while the total amount of twinning changes little on unloading there is substantial forward and reverse local twinning activity.

3.2. Texture memory

As we saw from figure 5(*d*), the twinning pattern produced by mechanical loading of a polycrystal in the α phase is not retained upon cycling through the phase transformation. That is, the material does not develop texture memory. However, if the material is cycled repeatedly through the phase transformation, then the texture developed after the first cycle is reproduced after subsequent cycles (visually indistinguishable from the texture shown in figure 5(*d*)). The first $\beta \rightarrow \alpha$ transformation establishes a variant selection that is not changed by subsequent loading in the α phase. This is because the only plastic deformation mode in the α phase is the twinning mode and, because there is only one β variant, memory of twinning is erased on transformation to the β phase. For the simulation results in figure 5, the texture changes from part (*a*) to part (*d*) because we simulate the first pass of the material through the phase transformation, establishing the initial $\beta \rightarrow \alpha$ variant selection. Selection is based on the local stress states as the grains transform from β to α. Given the paucity of plastic deformation mechanisms, when the material is unloaded it always has the same local stresses as temperature is lowered through the $\beta \rightarrow \alpha$ transformation.

Variant selection on $\beta \rightarrow \alpha$ transformation would be changed if the transformation occurred under applied load or if the material were deformed plastically by some other mechanism, such as dislocation glide within the β phase. Plastic deformation in the β phase can occur at higher temperatures by dislocation glide mechanisms [3], and such plastic deformation could result in a different stress state on subsequent $\beta \rightarrow \alpha$ transformation and thus in different α variant selection. Applied load would similarly change the stress state and affect variant selection.

Before we can adequately treat observed texture memory in natural samples [41], we need to better understand their initial state of residual stress and how it is established. Recall that for the simulations of novaculite, we assumed that there were no residual stresses in the material at 300 K. This may not be the case for samples with non-uniform textures.

4. Discussion

In summary, the model qualitatively reproduces the following experimentally observed effects:

- Under compression, twinning reduces the density of trigonal $(0\,2\,\bar{2}\,1)$ poles and increases the density of trigonal $(2\,0\,\bar{2}\,1)$ poles in the vicinity of the compression axis.
- At a given temperature, the amount of twinning increases gradually with applied load, with an initial lag and a decrease in the rate of twinning with applied load at higher loads.
- For a given applied stress level, there are increased amounts of twinning as the temperature is increased.
- Selective texture memory is exhibited, with texture from mechanically induced twinning lost upon $\alpha \leftrightarrow \beta$ temperature cycling.

It is satisfying that the model is able to reproduce many experimentally observed phenomena. This ability is due in considerable measure to the inclusion of elastic anisotropy and lattice strain effects in the driving force; effects that are typically not included in continuum phase transformation models.

The model and simulations here serve to highlight the importance of local stress state in quartz for twinning and for α variant selection upon $\beta \rightarrow \alpha$ transformation. Using a uniform deformation linking assumption versus finite element discretization of the aggregate gives qualitatively different behaviour, particularly for the reversal of twinning upon unloading. The finite element simulations account for local stress variations and are deemed to have higher

fidelity. The importance of local residual stress state for activation of plastic deformation modes has also been observed in other materials, such as beryllium [42] which, like quartz, develops residual stresses in part from thermal anisotropy.

Further work is planned to investigate the $\alpha \leftrightarrow \beta$ transformation and texture memory effects in more detail. All simulations here started from a uniform initial texture, and texture memory on $\alpha \leftrightarrow \beta$ cycling has so far only been experimentally observed for textured samples [41]. Further studies may be able to determine the relative importance of initial texture and grain scale residual stress state in producing texture memory. It is likely that refinements will have to be made to the phase transformation model. With the current model and material parameters, the temperature hysteresis of the phase transformation is too high compared with experimental observations [27]. The current model and parameters also predict more curvature in the stress/temperature phase boundary than is reported by [35].

Acknowledgments

This work was performed under the auspices of the US Department of Energy by the University of California, Lawrence Livermore National Laboratory under Contract W-7405- Eng-48 (UCRL-JRNL-220522). HRW is appreciative of support from NSF (EAR 0337006) and DOE-BES (DE-FG02-05ER15637) and IGPP-LLNL.

References

[1] Frondel C 1945 Secondary Dauphine twinning in quartz *Am. Mineral.* 447–68
[2] Thomas L A and Wooster W A 1951 Piezocrescense—the growth of dauphiné twinning in quartz under stress *Proc. R. Soc. Lond. Ser.* A **208** 43–62
[3] Tullis J 1970 Quartz: preferred orientation in rocks produced by Dauphiné twinning *Science* **168** 1342–4
[4] Pehl J and Wenk H-R 2005 Evidence for regional Dauphiné twinning in quartz from the Santa Rosa mylonite zone in southern California. A neutron diffraction study *J. Struct. Geol.* **27** 1741–9
[5] Trepmann C A and Spray J G 2005 Planar microstructures and Dauphiné twins in shocked quartz from the Charlevoix impact structure, Canada *Large Meteorite Impacts III Special Papers* vol 384 (Boulder, CO: Geological Society of America) pp 315–28
[6] Wenk H-R, Lonardelli I, Vogel S C and Tullis J 2005 Dauphiné twinning as evidence for an impact origin of preferred orientation in quartzite: an example from Vredefort, South Africa *Geology* **33** 273–6
[7] Wenk H-R, Rybacki E, Dresen G, Lonardelli I, Barton N, Franz H and Gonzalez G 2007 Dauphiné twinning and texture memory in polycrystalline quartz: 1. Experimental deformation of novaculite *Phys. Chem. Miner.* **33** 667–76
[8] MacDonald G J F 1957 Thermodynamics of solids under nonhydrostatic stress with geologic applications *Am. J. Sci.* **255** 266
[9] Barton N R, Benson D J and Becker R C 2003 A crystal level model for phase transformation allowing for large volume changes *Dislocations, Plasticity and Metal Forming; Proceedings of Plasticity '03: The Tenth International Sympoisum on Plasticity and its Current Applications* ed A S Khan (Fulton, MD: Neat Press) pp 412–14
[10] Barton N R, Benson D J and Becker R 2005 Crystal level continuum modelling of phase transformations: the $\alpha \leftrightarrow \epsilon$ transformation in iron *Modelling Simul. Mater. Sci. Eng.* **13** 707–31
[11] Jannetti C, Bassani J L and Turteltaub S 2005 Thermodynamic driving forces for martensitic phase transformations in shape-memory alloys *Mechanically Active Materials (Materials Research Society Symposium Proceedings* vol 855E*)* ed K J Van Vliet *et al* (Warrendale, PA: Materials Research Society) p W5.2
[12] Caspersen K J, Lew A, Ortiz M and Carter E A 2004 Importance of shear in the bcc-to-hcp transformation in iron *Phys. Rev. Lett.* **93** 115501
[13] Idesman A V, Levitas V I and Stein E 2000 Structural changes in elastoplastic material: a unified finite-element approach to phase transformation, twinning and fracture *Int. J. Plast.* **16** 893–949
[14] Yano K and Horie Y 2002 Mesomechanics of the α-ϵ transition in iron *Int. J. Plast.* **18** 1427–46

[15] Tullis J and Tullis T E 1974 Preferred orientation produced by mechanical Dauphiné twinning. Thermodynamics and axial experiments *Am. Geophys. Union Monogr.* **16** 67–82
[16] Ericksen J L 2001 On the theory of the α-β phase transition in quartz *J. Elast.* **63** 61–86
[17] Kihara K 2001 Molecular dynamics interpretation of structural changes in quartz *Phys. Chem. Miner.* **28** 365–76
[18] Levitas V I 1998 Thermomechanical theory of martensitic phase transformations in inelastic materials *Int. J. Solids Struct.* **35** 889–940
[19] Abeyaratne R and Knowles J K 1990 On the driving traction acting on a surface of strain discontinuity in a continuum *J. Mech. Phys. Solids* **38** 345–60
[20] Fischer F D, Reisner G, Werner E, Tanaka K, Cailletaud G and Antretter T 2000 A new view on transformation induced plasticity (TRIP) *Int. J. Plast.* **16** 723–48
[21] Anand L and Gurtin M E 2003 Thermal effects in the superelasticity of crystalline shape-memory materials *J. Mech. Phys. Solids* **51** 1015–58
[22] Kocks U F, Argon A S and Ashby M F 1975 Thermodynamics and kinetics of slip *Prog. Mater. Sci.* **19** 1–288
[23] Porter D A and Easterling K E 1992 *Phase Transformations in Metals and Alloys* (London: Chapman and Hall)
[24] Follansbee P S and Kocks U F 1988 A constitutive description of the deformation of copper based on the use of the mechanical threshold stress as an internal state variable *Acta Metall.* **36** 81–93
[25] Smirnov M B and Mirgorodsky A P 1997 Lattice-dynamical study of the α-β phase transition of quartz: soft-mode behavior and elastic anomalies *Phys. Rev. Lett.* **78** 2413–16
[26] Kimizuka H, Kaburaki H and Kogure Y 2003 Molecular-dynamics study of the high-temperature elasticity of quartz above the α-β phase transition *Phys. Rev.* B (Article) **67** 024105
[27] Sorrell C A, Anderson H U and Ackermann R J 1974 Thermal expansion and the high-low transformation in quartz: II. Dilatometric studies *J. Appl. Crystallogr.* **7** 468–73
[28] Ghosh G and Olson G B 1994 Kinetics of F.C.C.→B.C.C heterogeneous martensitic nucleation: II. Thermal activation *Acta Metall. Mater.* **42** 3371–9
[29] Abeyaratne R and Knowles J K 1993 A continuum model for a thermoelastic solid capable of undergoing phase transitions *J. Mech. Phys. Solids* **41** 541–71
[30] Diani J M and Parks D M 1998 Effects of strain state on the kinetics of strain-induced martensite in steels *J. Mech. Phys. Solids* **46** 1613–35
[31] Grujicic M and Zhang Y 2000 Crystal plasticity analysis of stress-assisted martensitic transformation in Ti-10V-2Fe-3Al (wt.%) *J. Mater. Sci.* **35** 4635–47
[32] Marketz W T, Fischer F D and Clemens H 2003 Deformation mechanisms in tial intermetallics—experiments and modeling *Int. J. Plast.* **19** 281–321
[33] Hearmon R F S 1956 The elastic constants of anisotropic materials—II *Adv. Phys.* 323–82
[34] Aleksandrov K S and Ryzhova T V 1961 The elastic properties of cyrstals *Sov. Phys.—Crystallogr.* **6** 228–52
[35] Coe R S and Patterson M S 1969 The α-β inversion in quartz: a coherent phase transition under nonhydrostatic stress *J. Geophys. Res.* **74** 4921–48
[36] Ohno I 1995 Temperature variation of elastic properties of α-quartz up to α-β transition *J. Phys. Earth* **43** 157–69
[37] Kihara K 1990 An X-ray study of the temperature dependence of the quartz structure *Eur. J. Mineral.* **2** 63–77
[38] Fletcher R 1987 *Practical Methods of Optimization* 2nd edn (New York: Wiley)
[39] Anderson A, Cooper R, Neely R, Nichols A, Sharp R and Wallin B 2003 Users manual for ALE3D—an arbitrary Lagrange/Eulerian 3D code system *Technical Report* UCRL-MA-152204, Lawrence Livermore National Laboratory
[40] Kocks U F, Tomé C N and Wenk H-R (ed) 1998 *Texture and Anisotropy: Preferred Orientations in Polycrystals and their Effect on Materials Properties* (Cambridge: Cambridge University Press)
[41] Wenk H-R 2006 Neutron diffraction texture analysis *Neutron Scattering in Earth Sciences (Reviews in Mineralogy and Geochemistry* vol 63*)* ed H-R Wenk (Mineralogical Society of America) (chapter 15) pp 399–426
[42] Brown D W, Bourke M A M, Clausen B, Holden T M, Tomé C N and Varma R 2003 A neutron diffraction and modeling study of uniaxial deformation in polycrystalline beryllium *Metall. Mater. Trans.* A **34** 1439–49